

Abstract

**Measurement of the positive kaon-argon total  
hadronic differential cross section in the LArIAT  
experiment**

Elena Gramellini

2018

Abstract goes here. Limit 750 words.

Measurement of the positive kaon-argon  
total hadronic differential cross section in  
the LArIAT experiment

A Dissertation  
Presented to the Faculty of the Graduate School  
of  
Yale University  
in Candidacy for the Degree of  
Doctor of Philosophy

by  
Elena Gramellini

Dissertation Director: Bonnie T. Fleming

Date you'll receive your degree

Copyright © 2017 by Elena Gramellini  
All rights reserved.

# Contents

|   |           |
|---|-----------|
| <b>Acknowledgements</b>   | <b>ix</b> |
| <b>1 Introduction</b>   | <b>1</b>  |
| 1.1 The Standard Model . . . . .  | 1         |
| 1.2 Neutrinos: in and beyond the Standard Model . . . . .               | 3         |
| 1.2.1 Neutrino in the SM . . . . .                                      | 3         |
| 1.2.2 Neutrino Oscillations . . . . .                                   | 5         |
| 1.3 Beyond the Standard Model . . . . .                                 | 6         |
| <b>2 Liquid Argon Detectors at the Intensity Frontier</b>               | <b>8</b>  |
| 2.1 The SBN Program . . . . .   | 9         |
| 2.1.1 SBN Goals . . . . .   | 9         |
| 2.1.2 Neutrino Interactions and Detection . . . . .                     | 9         |
| 2.2 DUNE . . . . .  | 9         |
| 2.2.1 DUNE Non-Accelerator Physics Program . . . . .                    | 9         |
| 2.2.2 Rare Decay Searches: Experimental Limit . . . . .                 | 9         |
| 2.2.3 Nucleon Decay Detection in LAr . . . . .                          | 9         |
| 2.3 Liquid Argon Time Projection Chambers at the Intensity Frontier . . | 9         |
| 2.3.1 Time Projection Chamber . . . . .                                 | 9         |
| 2.3.2 Ionization Detectors with Noble Liquids . . . . .                 | 9         |
| 2.3.3 LArTPC: Principles of Operation . . . . .                         | 9         |

|          |   |           |
|----------|---|-----------|
| 2.3.4    | Liquid Argon Ionization Charge Detection . . . . .      | 9         |
| 2.3.5    | Liquid Argon scintillation Light Detection . . . . .    | 9         |
| <b>3</b> | <b>LArIAT: Liquid Argon In A Testbeam</b>               | <b>10</b> |
| 3.1      | LArIAT & the Intensity Frontier . . . . .               | 11        |
| 3.2      | Testbeam and Beamline Detectors . . . . .               | 11        |
| 3.3      | In the Cryostat . . . . .                               | 11        |
| 3.3.1    | TPC: Charge Collection . . . . .                        | 11        |
| 3.3.2    | TPC: Light Collection System . . . . .                  | 11        |
| 3.3.3    | Cryogenics and Purity Control . . . . .                 | 11        |
| 3.3.4    | TPC: Electric Field Measurement . . . . .               | 11        |
| 3.4      | Trigger and DAQ . . . . .                               | 11        |
| 3.5      | Control Systems . . . . .                               | 11        |
| <b>4</b> | <b>Kaons Interactions in Argon: Cross Section</b>       | <b>12</b> |
| 4.1      | Literature Review . . . . .                             | 12        |
| 4.2      | How to Measure Hadron Cross Section in LArIAT . . . . . | 12        |
| 4.2.1    | Particle Selection . . . . .                            | 12        |
| 4.2.2    | Beamline to TPC Handshake . . . . .                     | 12        |
| 4.2.3    | The Thin Slice Method . . . . .                         | 12        |
| 4.2.4    | Procedure testing with truth quantities . . . . .       | 16        |
| <b>5</b> | <b>Data Collection</b>                                  | <b>18</b> |
| <b>6</b> | <b>LArIAT Monte Carlo</b>                               | <b>19</b> |
| 6.1      | Beamline . . . . .                                      | 19        |
| 6.1.1    | G4Beamline . . . . .                                    | 19        |
| 6.1.2    | Data Driven MC . . . . .                                | 19        |
| 6.2      | TPC MC . . . . .  | 19        |

|          |  |           |
|----------|--|-----------|
| <b>7</b> | <b>Energy Calibration</b>                                  | <b>20</b> |
| <b>8</b> | <b>Tracking Optimization</b>                               | <b>21</b> |
| 8.1      | MC sample and WC2TPC match . . . . .                       | 21        |
| 8.2      | Wire chamber-to-TPC match . . . . .                        | 22        |
| 8.2.1    | Wire chamber-to-TPC match: importance and definition . . . | 22        |
| 8.2.2    | Matching optimization . . . . .                            | 23        |
| 8.2.3    | Porting optimization to data . . . . .                     | 25        |
| <b>9</b> | <b>Kaon Cross Section Measurement</b>                      | <b>26</b> |
| <b>A</b> | <b>Measurement of LArIAT Electric Field</b>                | <b>27</b> |
| <b>B</b> | <b>Construction of A Cosmic Ray Tagger for MicroBooNE</b>  | <b>35</b> |
| <b>C</b> | <b>Pion Analysis</b>                                       | <b>36</b> |
| C.0.1    | Data Sample . . . . .                                      | 36        |
| C.0.2    | Capture and Decay . . . . .                                | 36        |

# List of Figures

|     |   |    |
|-----|---|----|
| 4.1 | Hadronic cross sections for $\pi^-$ -Ar (left) and $K^+$ -Ar (right) implemented in Geant4 10.01.p3 (solid lines) overlaid the true MC cross section as obtained with the sliced TPC method (markers). The total cross section is shown in green, the elastic cross section in blue and the inelastic cross section in red. . . . . | 17 |
| 8.1 | Efficiency (left) and purity (right) for wire chamber-to-TPC match as a function of the radius and angle selections. . . . .  | 25 |
| A.1 | Drift velocity dependence on electric field for several temperatures. The slope of the line at any one point represents the electron mobility for that given temperature and electric field. . . . .  | 28 |
| A.2 | <del>get rid of current line</del> LArIAT HV simple schematics. . . . .   | 29 |
| A.3 | <del>the axis is wrong!!</del> Current reading from the Glassman between May 25th and May 30th, 2016 (typical Run-II conditions). . . . .   | 29 |
| A.4 | Pictorial representation of the YX view of the TPC. The distance within the anode planes and between the shield plane and the cathode is purposely out of proportion to illustrate the time difference between hits on collection and induction. A ACP track is shown as an example.  | 33 |
| A.5 | Angle definition in the context of LArIAT coordinates system. . . . .   | 33 |

|     |   |    |
|-----|---|----|
| A.6 | Collection plane $\Delta t$ fit for Run II positive polarity ACP data selected tracks. . . . .  | 34 |
| A.7 | Induction plane $\Delta t$ fit for Run II positive polarity ACP data selected tracks. . . . .   | 34 |
| C.1 | True momentum distribution at wire chamber 4 for every simulated pion arriving in the TPC (pink), ending its life in capture (green) or in decay (blue) in the TPC, linear vertical axis on the left, logarithmic on the right. . . . . | 38 |
| C.2 | Survival ratio as a function of selection threshold on true momentum at wire chamber four for for every simulated pion arriving in the TPC (pink), capture (green) or in decay (blue). . . . .  | 39 |
| C.3 | Ratio between the capture (green) and decay (blue) events over the total number of events as a as a function of the true momentum at wire chamber four. . . . .   | 39 |



# List of Tables

|     |  |    |
|-----|--|----|
| 1.1 | SM elementary fermions. The subscripts L and R indicate respectively the negative helicity (left-handed) and the positive helicity (right-handed). | 2  |
| A.1 | Electric field and drift velocities in LArIAT smaller drift volumes . . .  | 28 |
| A.2 | $\Delta t$ for the different data samples used for the Anode-Cathode Piercing tracks study. . . . .  | 33 |
| C.1 | My caption . . . . .   | 37 |

# Acknowledgements

A lot of people are awesome. But not you, who are reading my thesis before it's done.

# Chapter 1

## Introduction

### 1.1 The Standard Model

The Standard Model (SM) of particle physics is the most accurate theoretical description of the subatomic world and, more generically, one of the most precisely tested theories in the history of physics. The SM describes the strong, electromagnetic and weak interactions among elementary particles in the framework of quantum field theory, accounting for the unification of electromagnetic and weak interactions for energies above the vacuum expectation value of the Higgs field. The SM does not describe gravity or general relativity.

The Standard Model is a gauge theory based on the local group of symmetry

$$G_{SM} = SU(3)_C \otimes SU(2)_T \otimes U(1)_Y \quad (1.1)$$

where the subscripts indicate the conserved charges: the strong charge, or color C, the weak isospin T (or rather its third component  $T_3$ ) and the hypercharge Y. These quantities can be related to the electric charge Q through the Gell-Mann-Nishijima relation:

$$Q = \frac{Y}{2} + T_3. \quad (1.2)$$

| Generation | I  | II   | III  | T   | Y  | Q   |
|------------|--|--|--|---|--|---|
| Leptons    | $\begin{pmatrix} \nu_e \\ e \end{pmatrix}_L$ | $\begin{pmatrix} \nu_\mu \\ \mu \end{pmatrix}_L$ | $\begin{pmatrix} \nu_\tau \\ \tau \end{pmatrix}_L$ | $\begin{matrix} 1/2 \\ -1/2 \end{matrix}$ | $\begin{matrix} -1 \\ -1 \end{matrix}$   | $\begin{matrix} 0 \\ -1 \end{matrix}$     |
|            | $e_R$  | $\mu_R$  | $\tau_R$   | 0   | -2                                       | 1   |
| Quarks     | $\begin{pmatrix} u \\ d' \end{pmatrix}_L$    | $\begin{pmatrix} c \\ s' \end{pmatrix}_L$        | $\begin{pmatrix} t \\ b' \end{pmatrix}_L$          | $\begin{matrix} 1/2 \\ -1/2 \end{matrix}$ | $\begin{matrix} 1/3 \\ 1/3 \end{matrix}$ | $\begin{matrix} 2/3 \\ -1/3 \end{matrix}$ |
|            | $u_R$  | $c_R$  | $t_R$  | 0   | $4/3$                                    | $2/3$                                     |
|            | $d'_R$                                       | $s'_R$   | $b'_R$   | 0   | $-2/3$                                   | $-1/3$                                    |

Table 1.1: SM elementary fermions. The subscripts L and R indicate respectively the negative helicity (left-handed) and the positive helicity (right-handed).

In the quantum field framework, the elementary particles correspond to the irreducible representations of the  $G_{SM}$  symmetry group. In particular, the particles are divided in two categories, fermions and bosons, according to their spin-statistics. Described by the Fermi-Dirac statistics, Fermions have half-integer spin and are sometimes called “matter-particles”. Bosons or “force carriers” have integer spin, follow the Bose-Einstein statistics and mediate the interaction between fermions. The fundamental fermions and their quantum numbers are listed in Tab 1.1.

Quarks can interact via all three the fundamental forces; they are triplets of  $SU(3)_C$ , that is they can exist in three different colors:  $C = R, G, B$ . If one chooses a base where  $u$ ,  $c$  and  $t$  quarks are simultaneously eigenstates of both the strong and the weak interactions, the remaining eigenstates are usually written as  $d$ ,  $s$  and  $b$  for the strong interaction and  $d'$ ,  $s'$  and  $b'$  for the weak interaction, because the latter ones are the result of a Cabibbo rotation on the first ones. Charged leptons interact via the weak and the electromagnetic forces, while neutrinos only interact via the weak force. The gauge group univocally determines the number of gauge bosons that carry the interaction; the gauge bosons correspond to the generators of

the group: eight gluons (g) for the strong interaction, one photon ( $\gamma$ ) and three bosons ( $W^\pm, Z^0$ ) for the electroweak interaction. A gauge theory by itself can not provide a description of massive particles, but it is experimentally well known that most of the elementary particles have non-zero masses. The introduction of massive fields in the Standard Model lagrangian would make the theory non-renormalizable, and - so far - mathematically impossible to handle. This problem is solved in the Standard Model by the introduction of a scalar iso-doublet  $\Phi(x)$ , the Higgs field, which gives mass to  $W^\pm$  and  $Z^0$  gauge bosons through the electroweak symmetry breaking and to the fermions through Yukawa coupling [1,2].

## 1.2 Neutrinos: in and beyond the Standard Model

### 1.2.1 Neutrino in the SM

Neutrino were introduced in the SM as left-handed massless Weyl spinors. The Dirac equation of motion

$$(i\gamma^\mu\partial_\mu - m)\psi = 0 \tag{1.3}$$

for a fermionic field

$$\psi = \psi_L + \psi_R \tag{1.4}$$

is equivalent to the equations

$$i\gamma^\mu\partial_\mu\psi_L = m\psi_R \tag{1.5}$$

$$i\gamma^\mu\partial_\mu\psi_R = m\psi_L \tag{1.6}$$

for the chiral fields  $\psi_R$  and  $\psi_L$ , whose evolution in space and time is coupled through the mass  $m$ . If the fermion is massless, the chiral fields decouple and the fermion can be described by a single Weyl spinor with two independent components. Pauli initially rejected the description of a physical particle through a single Weyl

spinor because of its implication of parity violation. In fact, since the spatial inversion operator throws  $\psi_R \leftrightarrow \psi_L$ , parity is conserved only if the both the chiral components exist at the same time. **ADD CITATIONS**. For the neutrino introduction in the SM, experiments came in help of the theoretical description: the constraint of parity conservation weakened after Wu's experiment **ADD CITATIONS AND DATES**, there was no experimental indication for massive neutrinos and neutrinos likely interacted only via the left-handed component.

The symmetry group  $SU(2)_T \otimes U(1)_Y$  is the only group relevant for neutrino interactions. The SM electroweak lagrangian is the most general renormalizable lagrangian invariant under the local symmetry group  $SU(2)_T \otimes U(1)_Y$ . The lagrangian couples the weak isotopic spin doublets and singlets described in 1.1 with the gauge bosons  $A_a^\mu$  ( $a = 1, 2, 3$ ) and  $B^\mu$ , and Higgs doublet  $\Phi(x)$ :

$$\begin{aligned}
\mathcal{L} = & i \sum_{\alpha=e,\mu,\tau} \bar{L}'_{\alpha L} \not{D} L'_{\alpha L} + i \sum_{\alpha=1,2,3} \bar{Q}'_{\alpha L} \not{D} Q'_{\alpha L} \\
& + i \sum_{\alpha=e,\mu,\tau} \bar{l}'_{\alpha R} \not{D} l'_{\alpha R} + i \sum_{\alpha=d,s,b} \bar{q}'^D_{\alpha R} \not{D} q'^D_{\alpha R} + i \sum_{\alpha=u,c,t} \bar{q}'^U_{\alpha R} \not{D} q'^U_{\alpha R} \\
& - \frac{1}{4} A_{\mu\nu} A^{\mu\nu} - \frac{1}{4} B_{\mu\nu} B^{\mu\nu} \\
& + (D_\rho \Phi)^\dagger (D^\rho \Phi) - \mu^2 \Phi^\dagger \Phi - \lambda (\Phi^\dagger \Phi)^2 \\
& - \sum_{\alpha,\beta=e,\mu,\tau} \left( Y_{\alpha\beta}^n \bar{L}'_{\alpha L} \Phi l'_{\beta R} + Y_{\alpha\beta}^{n*} \bar{l}'_{\beta R} \Phi^\dagger L'_{\alpha L} \right) \\
& - \sum_{\alpha=1,2,3} \sum_{\beta=d,s,b} \left( Y_{\alpha\beta}^D \bar{Q}'_{\alpha L} \Phi q'^D_{\beta R} + Y_{\alpha\beta}^{D*} \bar{q}'^D_{\beta R} \Phi^\dagger Q'_{\alpha L} \right) \\
& - \sum_{\alpha=1,2,3} \sum_{\beta=u,c,t} \left( Y_{\alpha\beta}^U \bar{Q}'_{\alpha L} \tilde{\Phi} q'^U_{\beta R} + Y_{\alpha\beta}^{U*} \bar{q}'^U_{\beta R} \tilde{\Phi}^\dagger Q'_{\alpha L} \right). \tag{1.7}
\end{aligned}$$

The first two lines of the lagrangian summarize the kinetic terms for the fermionic fields and their coupling to the gauge bosons  $A_a^{\mu\nu}$ ,  $B^{\mu\nu}$ <sup>1</sup>. The third line describes

---

1. In gauge theories the ordinary derivative  $\partial_\mu$  is substituted with the covariant derivative  $D_\mu$ . Here  $D_\mu = \partial_\mu + ig A_\mu \cdot I + ig' B_\mu \frac{Y}{2}$ , where  $I$  and  $Y$  are the  $SU(2)_L$  and  $U(1)_Y$  generators, respectively.

the kinetic terms and the self-coupling terms of the gauge bosons. The forth line is the Higgs lagrangian, which results in the spontaneous symmetry breaking. The last three lines describe the Yukawa coupling between fermions and the Higgs field, origin of the fermion's mass.

The coupling between left-handed and right-handed field generates the mass term for fermions. The SM assumes only left-handed components for neutrinos, thus implying zero neutrino mass. Since any linear combination of massless fields results in a massless field, the flavor eigenstates are identical to the mass eigenstates in the SM.

### 1.2.2 Neutrino Oscillations

The determination of the flavor of a neutrino dynamically arises from the corresponding charged lepton associated in a CC interaction; for example, a  $\nu_e$  is a neutrino which produces an  $e^-$ , a  $\bar{\nu}_\mu$  is a neutrino which produces a  $\mu^+$ , *etc.* The neutrino flavor eigenstates  $|\nu_\alpha\rangle$ , with  $\alpha = e, \mu, \tau$ , are orthogonal to each other and form a base for the the weak interaction matrix.

Overwhelming experimental data show neutrinos change flavor during their propagation. This phenomenon, predicted by Bruno Pontecorvo in 1957, is called “neutrino oscillations” and it is possible only if the flavor eigenstate are not identical to the mass eigenstates. A minimal extension of the Standard Model introduces three mass eigenstates,  $|\nu_i\rangle$  ( $i = 1, 2, 3$ ), whose mass  $m_i$  is well defined. The unitary Pontecorvo-Maki-Nakagawa-Sakata matrix transforms the spinor wave functions ( $\psi$ ) of each component between flavor and mass bases as follows

$$\sum \psi_\alpha |\nu_\alpha\rangle = \sum \psi_i |\nu_i\rangle, \rightarrow \psi_\alpha = U_{PMNS} \psi_i, \quad (1.8)$$

with

$$U_{PMNS} = \begin{bmatrix} c_{12} & s_{12} & 0 \\ -s_{12} & c_{12} & 0 \\ 0 & 0 & 1 \end{bmatrix} \begin{bmatrix} c_{13} & 0 & s_{13}e^{-i\delta} \\ 0 & 1 & 0 \\ -s_{13}e^{-i\delta} & 0 & c_{13} \end{bmatrix} \begin{bmatrix} 1 & 0 & 0 \\ 0 & c_{23} & s_{23} \\ 0 & -s_{23} & c_{23} \end{bmatrix} \begin{bmatrix} e^{i\alpha_1} & 0 & 0 \\ 0 & e^{i\alpha_2} & 0 \\ 0 & 0 & 1 \end{bmatrix} \quad (1.9)$$

where  $c$  e  $s$  stand respectively for cosine and sine of the corresponding mixing angles ( $\theta_{12}$ ,  $\theta_{23}$  and  $\theta_{13}$ ),  $\delta$  is the Dirac CP violation phase,  $\alpha_1$  and  $\alpha_2$  is the eventual Majorana CP violation phases.

### Experimental results summary

## 1.3 Beyond the Standard Model

The discovery of neutrino oscillation and its implication of non-zero neutrino mass mark the beginning of a new, exciting era in neutrino physics: the era of physics Beyond the Standard Model (BSM) in the neutrino sector. We are currently searching for new, deeper theories that can accommodate neutrinos with non-zero mass, while remaining consistent with the rest of the Standard Model.

### Open Questions in Neutrino Physics

On one hand, the last X decades of experiments in neutrino oscillations brought spectacular advancements in the understanding of the oscillations pattern, measuring the neutrino mixing angles and mass splitting with a precision of less than 10%. On the other, it opened the field for a series of questions needing experimental answers. Critical challenges in the next decade will entail an even deeper understanding of the neutrino mixing pattern, investigation of the neutrino mass origin, neutrino number and nature, and assessing CP violation in the lepton sector.

Following the recommendation of the latest Particle Physics Project Prioritization



Panel [3], the US is dedicating substantial resources to the development of a short- and long- baseline neutrino program to address many of these fundamental questions. This program pivots on the Liquid Argon Time Projection Chamber (LArTPC) detector technology which will be described in 2.

The main goals of these research programs include:

- Assessment of the existence of right-handed sterile neutrinos.
- Determination of the sign of  $\Delta m_{13}^2$  (or  $\Delta m_{23}^2$ ), i.e., the “neutrino mass ordering”.
- Determination of the octant, i.e. whether  $\theta_{23}$  is maximal.
- Determination the status of CP symmetry in the lepton sector.

**Smallness of neutrino masses, link to GUTs**

### **Towards a more fundamental theory**

Despite its highly predictive power, a number of conceptual issues arise in the SM which disfavor it to be a good candidate for a fundamental theory.

The SM rather complex group structure, where a gauge group is formed with the direct product of other three groups as shown in eq. 1.1, is unexplained. Also, the SM fails to include a suitable dark matter candidate and a mechanisms that accounts for the baryon asymmetry of the universe. Within the SM, a total of 25 parameters remain seemingly arbitrary and need to be fitted to data: 3 gauge couplings, 9 charged fermion masses, 3 mixing angles and one CP phase in the CKM matrix, the Higgs mass and quartic coupling,  $\theta_{QCD}$ , 3 neutrino masses, 3 neutrino mixing angles, 1 Dirac phase and, eventually, 2 Majorana phases.

## Chapter 2

# Liquid Argon Detectors at the Intensity Frontier

In the next few years, LArTPC experiments – such as the Short-Baseline Neutrino program (SBN) and DUNE – will be major players in the intensity frontier field.

## **2.1 The SBN Program**

### **2.1.1 SBN Goals**

### **2.1.2 Neutrino Interactions and Detection**

## **2.2 DUNE**

### **2.2.1 DUNE Non-Accelerator Physics Program**

### **2.2.2 Rare Decay Searches: Experimental Limit**

### **2.2.3 Nucleon Decay Detection in LAr**

## **2.3 Liquid Argon Time Projection Chambers at the Intensity Frontier**

### **2.3.1 Time Projection Chamber**

### **2.3.2 Ionization Detectors with Noble Liquids**

### **2.3.3 LArTPC: Principles of Operation**

### **2.3.4 Liquid Argon Ionization Charge Detection**

Electron Life Time & purity

Space Charge Effect

Recombination Effect

### **2.3.5 Liquid Argon scintillation Light Detection**

LAr Scintillation Process

Wavelength Shifting of LAr Scintillation Light



# Chapter 3

## LArIAT: Liquid Argon In A Testbeam

### 3.1 LArIAT & the Intensity Frontier

### 3.2 Testbeam and Beamline Detectors

### 3.3 In the Cryostat

#### 3.3.1 TPC: Charge Collection

#### 3.3.2 TPC: Light Collection System

#### 3.3.3 Cryogenics and Purity Control

#### 3.3.4 TPC: Electric Field Measurement

### 3.4 Trigger and DAQ

### 3.5 Control Systems

# Chapter 4

## Kaons Interactions in Argon: Cross Section

### 4.1 Literature Review

### 4.2 How to Measure Hadron Cross Section in LAr-IAT

#### 4.2.1 Particle Selection

#### 4.2.2 Beamline to TPC Handshake

#### 4.2.3 The Thin Slice Method

#### Cross Sections on Thin Target

Cross section measurements on a thin target have been the bread and butter of nuclear and particle Iexperimentalists since the Rutherford experiments **NEED CITATION**. At their core, this type of experiments consists in shooting a beam of particles with a known flux on a thin target and recording the outgoing flux.

In general, the target is not a single particle, but rather a slab of material containing many diffusion centers. The so-called “thin target” approximation assumes that the target centers are uniformly distributed in the material and that the target is thin compared to the interaction length so that no center of interaction sits in front of another. In this approximation, the ratio between the number of particles interacting in the target  $N_{Interacting}$  and number of incident particles  $N_{Incident}$  determines the interaction probability  $P_{Interacting}$ , which is the complementary to one of the survival probability  $P_{Survival}$ . Equation 4.1

$$P_{Survival} = 1 - P_{Interacting} = 1 - \frac{N_{Interacting}}{N_{Incident}} = e^{-\sigma_{TOT}n\delta X} \quad (4.1)$$

describes the probability for a particle to survive the thin target. This formula relates the total cross section  $\sigma_{TOT}$ , the density of the target centers  $n$  and the thickness of the target along the incident hadron direction  $\delta X$ , to the interaction probability<sup>1</sup>. If the target is thin compared to the interaction length of the process considered, we can Taylor expand the exponential function in equation 4.1 and find a simple proportionality relationship between the number of incident and interacting particles, and the cross section, as shown in equation 4.2:

$$1 - \frac{N_{Interacting}}{N_{Incident}} = 1 - \sigma_{TOT}n\delta X + O(\delta X^2). \quad (4.2)$$

Solving for the cross section, we find:

$$\sigma_{TOT} = \frac{1}{n\delta X} \frac{N_{Interacting}}{N_{Incident}}. \quad (4.3)$$

---

1. The scattering center density in the target,  $n$ , relates to the argon density  $\rho$ , the Avogadro number  $N_A$  and the argon molar mass  $m_A$  as  $n = \frac{\rho N_A}{m_A}$ .

## Not-so-Thin Target: Slicing the Argon

The LArIAT TPC, with its 90 cm of length, is not a thin target. **Find expected interaction length for hadrons and kaons.** However, the fine-grained tracking of the LArIAT LArTPC allows us to treat the argon volume as a sequence of many adjacent thin targets.

As described in section 3, LArIAT wire planes count 240 wires each. The wires are oriented at  $\pm 60^\circ$  from the vertical direction at 4 mm spacing, while the beam direction is oriented 3 degrees off the  $z$  axis in the  $XZ$  plane. **review this math** The wires collect signals proportional to the energy loss of the hadron along its path in a  $\delta X = 4 \text{ mm} / \sin(60^\circ) \approx 4.7 \text{ mm}$  slab of liquid argon. Thus, one can think to slice the TPC into many thin targets of  $\delta X = 4.7 \text{ mm}$  thickness along the direction of the incident particle.

Considering each slice  $j$  a “thin target”, we can apply the cross section calculation from Eq. 4.3 iteratively, evaluating the kinetic energy of the hadron as it enters each slice,  $E_j^{kin}$ . For each WC-to-TPC matched particle, the energy of the hadron entering the TPC is known thanks to the momentum and mass determination by the tertiary beamline,

$$E_{FrontFace}^{kin} = \sqrt{p_{Beam}^2 - m_{Beam}^2} - E_{loss}, \quad (4.4)$$

where  $E_{loss}$  is a correction for the energy loss in the dead material between the beamline and the TPC front face (more on ??). The energy of the hadron at the each slab is determined by subtracting the energy released by the particle in the previous slabs. For example, at the  $j^{th}$  point of a track, the kinetic energy will be

$$E_j^{kin} = E_{FrontFace}^{kin} - \sum_{i < j} \Delta E_i, \quad (4.5)$$

where  $\Delta E_i$  is the energy deposited at each argon slice before the  $j^{th}$  point as measured



by the calorimetry associated with the tracking.

If the particle enters a slice, it contributes to  $N_{Incident}(E^{kin})$  in the energy bin corresponding to its kinetic energy in that slice. If it interacts in the slice, it then also contributes to  $N_{Interacting}(E^{kin})$  in the appropriate energy bin. The cross section as a function of kinetic energy,  $\sigma_{TOT}(E^{kin})$  will then be proportional to the ratio  $\frac{N_{Interacting}(E^{kin})}{N_{Incident}(E^{kin})}$ .

The statistical uncertainty for each energy bin is calculated by error propagation from the statistical uncertainty on  $N_{Incident}$  and  $N_{Interacting}$ . Since the number of incident hadrons in each energy bin is given by a simple counting, we assume that  $N_{Incident}$  is distributed as a poissonian with mean and  $\sigma^2$  equal to  $N_{Incident}$  in each bin. On the other hand,  $N_{Interacting}$  follows a binomial distribution: a particle in a given energy bin might or might not interact. The square of the variance for the binomial is given by

$$\sigma^2 = \mathcal{N} P_{Interacting} (1 - P_{Interacting}); \quad (4.6)$$

since the interaction probability  $P_{Interacting}$  is  $\frac{N_{Interacting}}{N_{Incident}}$  and the number of tries  $\mathcal{N}$  is  $N_{Incident}$ , equation 4.6 translates into

$$\sigma^2 = N_{Incident} \frac{N_{Interacting}}{N_{Incident}} \left(1 - \frac{N_{Interacting}}{N_{Incident}}\right) = N_{Interacting} \left(1 - \frac{N_{Interacting}}{N_{Incident}}\right). \quad (4.7)$$

$N_{Incident}$  and  $N_{Interacting}$  are not independent. The uncertainty on the cross section is thus calculated as

$$\delta\sigma_{tot}(E) = \sigma_{tot}(E) \left( \frac{\delta N_{Interacting}}{N_{Interacting}} + \frac{\delta N_{Incident}}{N_{Incident}} \right) \quad (4.8)$$

where:

$$\delta N_{Incident} = \sqrt{N_{Incident}} \quad (4.9)$$

$$\delta N_{Interacting} = \sqrt{N_{Interacting} \left(1 - \frac{N_{Interacting}}{N_{Incident}}\right)}. \quad (4.10)$$

#### 4.2.4 Procedure testing with truth quantities

The  $\pi^-$ -Ar and  $K^+$ -Ar total hadronic cross section implemented in Geant4 can be used as a tool to validate the measurement methodology. We describe here a closure test done on Monte Carlo to prove that the methodology of slicing the TPC retrieves the underlying cross section distribution implemented in Geant4 within the statistical error.

For pions in the considered energy range, **the Geant4 inelastic model adopted to is “BertiniCascade”, while the elastic model “hElasticLHEP”**. For kaons, the Geant4 inelastic model adopted to is “BertiniCascade”, while the elastic model “hElasticLHEP”.

For the validation test, we fire about 390000 pions and 140000 kaons inside the LArIAT TPC active volume using the DDMC (see sec 6.1.2). We apply the thin-sliced method on using true quantities to calculate the hadron kinetic energy at each slab in order to decouple reconstruction effects to eventual issues with the methodology. For each slab of 4.7 mm length on the path of the hadron, we integrate the true energy deposition as given by the Geant4 transportation model. Then, we recursively subtracted it from the hadron kinetic energy at the TPC front face to evaluate the kinetic energy at each slab until the true interaction point is reached. Doing so, we obtain the true interacting and incident distributions for the considered hadron and we obtain the true MC cross section as a function of the hadron true kinetic energy.

Figure 4.2.4 shows the total hadronic cross section for argon implemented in Geant4 10.01.p3 (solid lines) overlaid with the true MC cross section as obtained

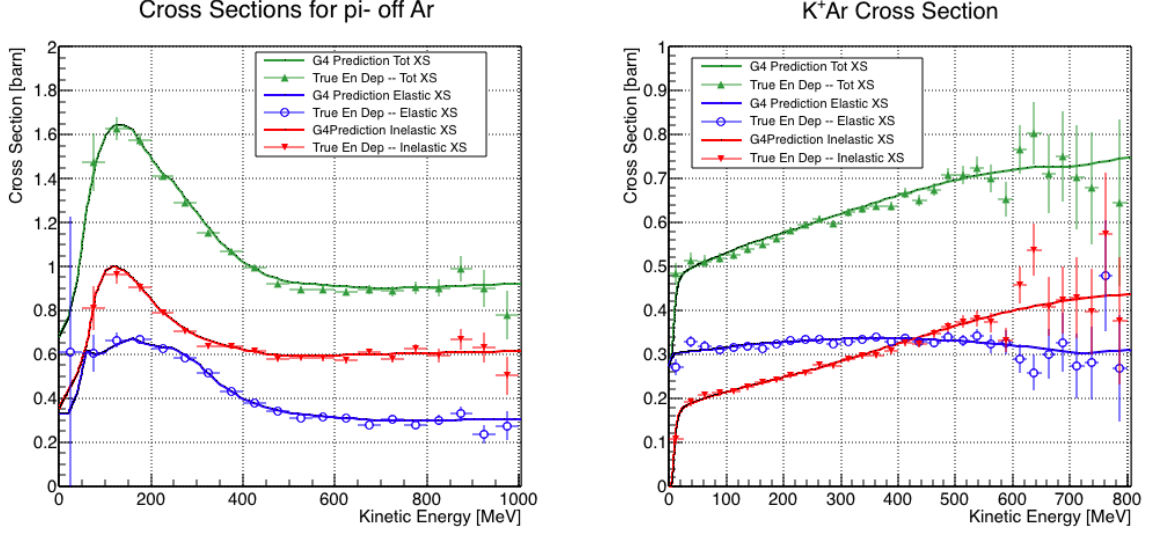


Figure 4.1: Hadronic cross sections for  $\pi^-$ -Ar (left) and  $K^+$ -Ar (right) implemented in Geant4 10.01.p3 (solid lines) overlaid the true MC cross section as obtained with the sliced TPC method (markers). The total cross section is shown in green, the elastic cross section in blue and the inelastic cross section in red.

with the sliced TPC method (markers) for pions on the left and kaons on the right; the total cross section is shown in green, the elastic cross section in blue and the inelastic cross section in red. The nice agreement with the Geant4 distribution and the cross section obtained with the sliced TPC method gives us confidence in the validity of the methodology.

# Chapter 5

## Data Collection

Your first chapter is probably an introduction. But who knows.

# Chapter 6

## LArIAT Monte Carlo

### 6.1 Beamline

#### 6.1.1 G4Beamline

#### 6.1.2 Data Driven MC

### 6.2 TPC MC

# Chapter 7

## Energy Calibration

Your first chapter is probably an introduction. But who knows.

# Chapter 8

## Tracking Optimization

Understanding how kaons and pions are tracked inside the TPC and optimizing the reconstruction algorithms to maximize the correct identification of the interaction point is a fundamental step of the analysis.

### 8.1 MC sample and WC2TPC match

The optimization is performed on a MC sample of 191000 kaons and 359000 pions produced with the DDMC technique. DDMC particles are shot from the WC4 location into the TPC following the beam profile. We mimic the matching between the WC and the TPC track on Monte Carlo by constructing a fake WC track using truth information at wire chamber four. We then apply the same WC to TPC matching algorithm as in data.

Plots I want in this section:

1. WC2TPC MC DeltaX, DeltaY and  $\alpha$
2. Delta L, reco - true
3. Delta L, reco - true Elastic, Delta L, reco - true Inelastic, other

4. Length Quality cut
5. Efficiency as a function of true KE and Angle

## 8.2 Wire chamber-to-TPC match

### 8.2.1 Wire chamber-to-TPC match: importance and definition

something something about why this match is important

In data, we attempt to uniquely match one WC-Track to one and only one reconstructed TPC track. This match is done by using in the  $X$  and  $Y$  coordinate of the extrapolated WC-Track to the upstream most point of the reconstructed TPC Track and by using the angle between the incoming track angle and the reconstructed TPC. We define  $\Delta X$  as the difference between the  $x$  position of the most upstream point of the TPC track and the  $x$  position of the WC track as projected to the TPC front face.  $\Delta Y$  is defined analogously. We define  $\Delta R$  as  $\Delta R = \sqrt{\Delta X^2 + \Delta Y^2}$ . The angle between the incident WC Track and the TPC track in the plane that contains them defines  $\alpha$ .

We define a match between WC-track and TPC reconstructed track if  $\Delta R < r_T$ ,  $\alpha < \alpha_T$  and the Z position of the first reconstructed point of the TPC track is within 2 cm from the TPC front face. The determination of the best  $r_T$  and  $\alpha_T$  is the scope of the following section.

In MC, we mimic the matching between the WC and the TPC track on Monte Carlo by constructing a fake WC track using truth information at wire chamber four. We then apply the same WC to TPC matching algorithm as in data.



## 8.2.2 Matching optimization

Scope of this optimization study is assessing the goodness of the wire chamber-to-TPC match on Monte Carlo and porting the optimized selection cuts to data. A word of caution is necessary here. With this study, we want to minimize pathologies associated with the presence of the primary kaon itself, like the incorrect association between the beamline kaon its decay products inside the TPC. Assessing the contamination from pile-up<sup>1</sup>, albeit related, is beyond the scope of this study.

In MC, we are able to define a correct WC2TPC match using the Geant4 truth information. We are thus able to count how many times the WC tracks is associated with the wrong TPC reconstructed track.

We define a correct match if the all following conditions are met:

- the length of the true primary Geant4 track in the TPC is greater than 2 cm,
- the length of the reconstructed track length is greater than 2 cm,
- the Z position of the first reconstructed point is within 2 cm from the TPC front face
- the distance between the reconstructed track and the true entering point is the minimum compared with all the other reconstructed tracks.

In order to count the wrong matches, we consider all the reconstructed tracks whose Z position of the first reconstructed point lies within 2 cm from the TPC front face. Events with true length in TPC  $< 2$  cm are included. Since kaons are shot 100 cm upstream from the TPC front face, the following two scenarios are possible from a truth standpoint:

[*Ta* ] the primary kaon decays or interact strongly before getting to the TPC,

---

1. We remind the reader that the DDMC is a single particle Monte Carlo, where the beam pile up is not simulated.

[ $Tb$ ] the primary kaon enters the TPC.

Once we choose the selection cuts to determine a reconstructed wire chamber-to-TPC match  $r_T$  and  $\alpha_T$ , the following four scenarios are possible :

- 1) no reconstructed tracks are matched
- 2) the correct track and one (or more) wrong tracks are matched
- 3) only the correct track is matched
- 4) one (or more) wrong track is matched.

If we keep only events with one and only one match, we discard cases 1) and 2) from the cross section measurement. For each set of  $r_T$  and  $\alpha_T$  selection value, we define purity and efficiency of the selection as follows:

$$\text{Efficiency} = \frac{\text{Number of events correctly matched}}{\text{Number of events with primary in TPC}} \quad (8.1)$$

$$\text{Purity} = \frac{\text{Number of events correctly matched}}{\text{Total number of matched events}}. \quad (8.2)$$

Figure 8.1 shows the efficiency (left) and purity (right) for wire chamber-to-TPC match as a function of the radius,  $r_T$ , and angle,  $\alpha_T$ , selection value. It is apparent how both efficiency and purity are fairly flat as a function of the radius selection value at a given angle. This is not surprising, given the fact that the wrong matches can occur in a single particle gun MC only for mis-tracking of the primary or for association with decay products, which are generally different in angle, but might be more similar in  $x$  and  $y$  projection. The radius cut would play a key role in removing pile up events.

For LArIAT cross section measurements, we generally prefer purity over efficiency, since a sample of particle of a pure species will lead to a better measurement. In the

case of kaons however, efficiency needs not to drop too low, given the smallness of the kaon sample. We choose  $(\alpha_T, r_T) = (8 \text{ deg}, 4 \text{ cm})$  and get a MC 85% efficiency and 98% purity.

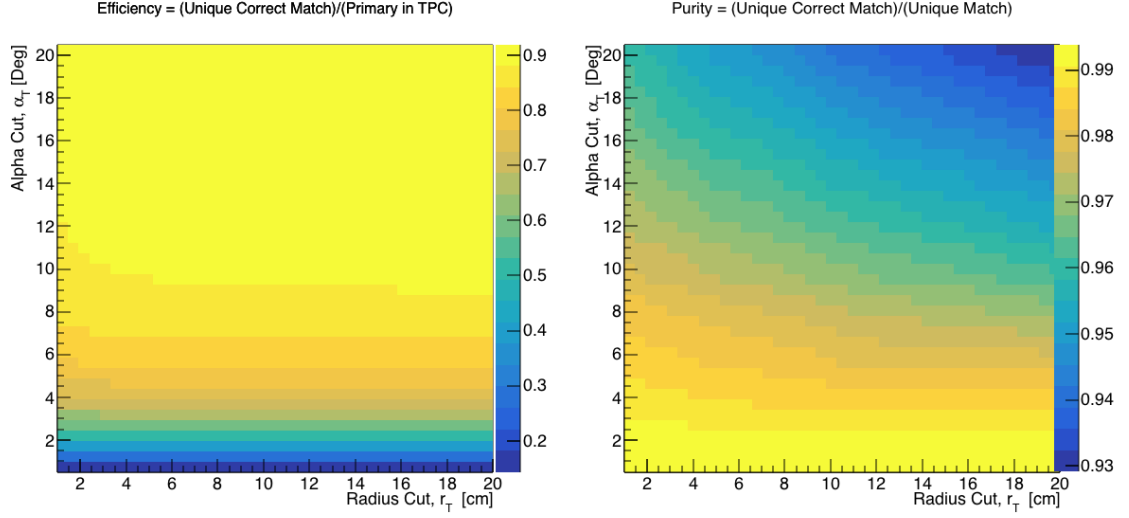


Figure 8.1: Efficiency (left) and purity (right) for wire chamber-to-TPC match as a function of the radius and angle selections.

### 8.2.3 Porting optimization to data

## Chapter 9

# Kaon Cross Section Measurement

Your first chapter is probably an introduction. But who knows.

# Appendix A

## Measurement of LArIAT Electric Field

The electric field of a LArTPC in the drift volume is a fundamental quantity for the proper functionality of this technology, as it affects almost every reconstructed quantity such as the position of hits or their collected charge. Given its importance, we calculate the electric field for LArIAT with a single line diagram from our HV circuit and we cross check the obtained value with a measurement relying only on TPC data.

Before getting into the details of the measurement procedures, it is important to explicit the relationship between some quantities in play. The electric field and the drift velocity ( $v_{drift}$ ) are related as follows

$$v_{drift} = \mu(E_{field}, T)E_{field}, \tag{A.1}$$

where  $\mu$  is the electron mobility, which depends on the electric field and on the temperature (T). The empirical formula for this dependency is described in [?] and shown in Figure A.1 for several argon temperatures.

The relationship between the drift time ( $t_{drift}$ ) and the drift velocity is trivially

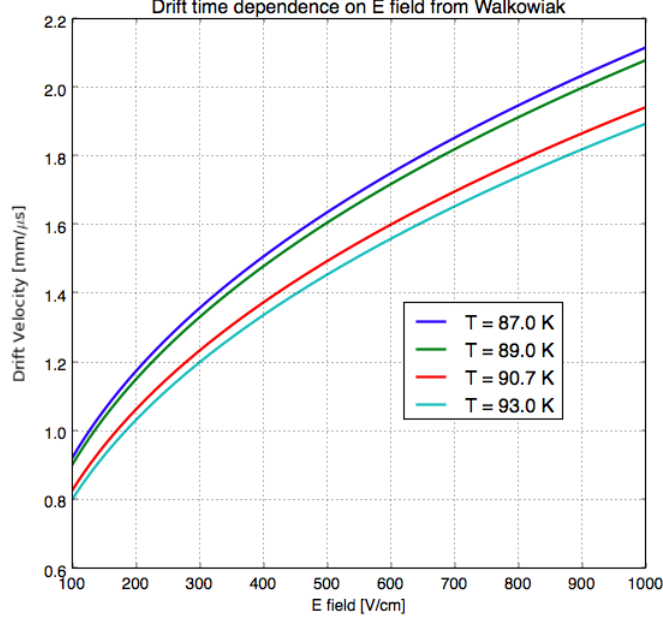


Figure A.1: Drift velocity dependence on electric field for several temperatures. The slope of the line at any one point represents the electron mobility for that given temperature and electric field.

Table A.1: Electric field and drift velocities in LArIAT smaller drift volumes

|             | Shield-Induction | Induction-Collection |
|-------------|------------------|----------------------|
| $E_{field}$ | 700.625 V/cm     | 892.5 V/cm           |
| $v_{drift}$ | 1.73 mm/ $\mu$ s | 1.90 mm/ $\mu$ s     |
| $t_{drift}$ | 2.31 $\mu$ s     | 2.11 $\mu$ s         |

given by

$$t_{drift} = \Delta x / v_{drift}, \quad (\text{A.2})$$

where  $\Delta x$  is the distance between the edges of the drift region. Table A.1 reports the values of the electric field, drift velocity, and drift times for the smaller drift volumes.

With these basic parameters established, we can now move on to calculating the electric field in the main drift region (between the cathode and the shield plane).

## Single line diagram method

The electric field strength in the LArIAT main drift volume can be determined knowing the voltage applied to the cathode, the voltage applied at the shield plane, and the distance between them. We assume the distance between the cathode and the shield plane to be 470 mm and any length contraction due to the liquid argon is negligibly small ( $\sim 2$  mm).

The voltage applied to the cathode can be calculated using Ohm's law and the single line diagram shown in Figure A.2. A set of two of filter pots for emergency power dissipation are positioned between the Glassman power supply and the cathode, one at each end of the feeder cable, each with an internal resistance of  $40\text{ M}\Omega$ . The output current of the Glassman power supply is then used to determine the electric field strength. Figure A.3 shows an average current of  $0.004172\text{ mA}$  from the Glassman power supply.

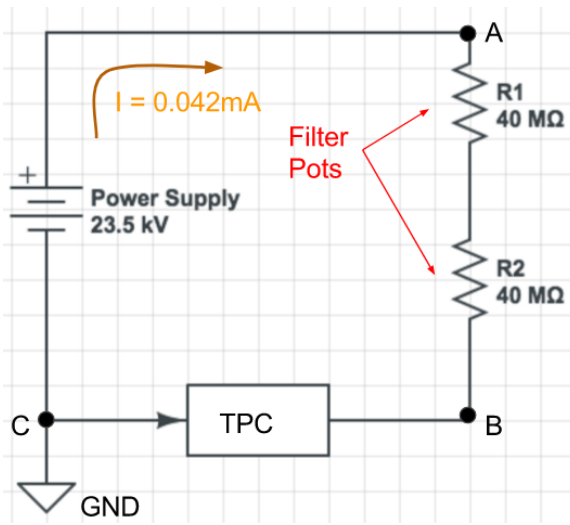


Figure A.2: ~~get rid of current line~~ LAr-IAT HV simple schematics.

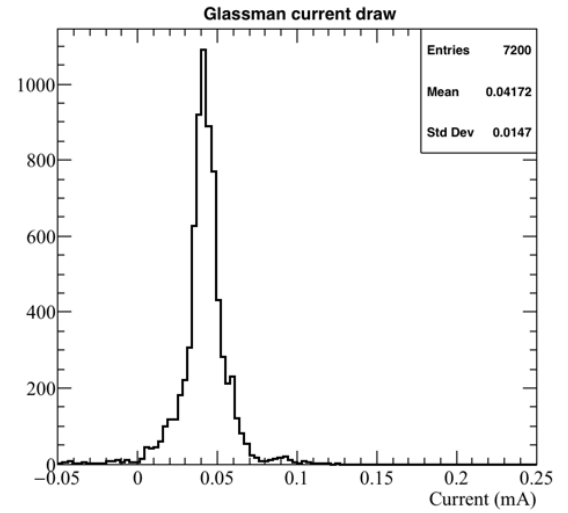


Figure A.3: ~~the axis is wrong!!~~ Current reading from the Glassman between May 25th and May 30th, 2016 (typical Run-II conditions).

Using this current, the voltage at the cathode is calculated as

$$V_{BC} = V_{PS} - (I \times R_{eq}) = -23.5 \text{ kV} + (0.00417 \text{ mA} \times 80 \text{ M}\Omega) = -23.17 \text{ kV}, \quad (\text{A.3})$$

where  $I$  is the current and  $R_{eq}$  is the equivalent resistor representing the two filter pots. The electric field, drift voltage, and drift time are then calculated to be

$$E_{\text{field}} = \frac{V_{BC} - V_{\text{shield}}}{\Delta x} = 486.54 \text{ V/cm} \quad (\text{A.4})$$

## E field using cathode-anode piercing tracks

We devise an independent method to measure the drift time (and consequently drift velocity and electric field) using TPC cathode to anode piercing tracks. We use this method as a cross check to the single line method. The basic idea is simple:

0. Select cosmic ray events with only 1 reconstructed track
1. Reduce the events to the one containing tracks that cross both anode and cathode
2. Identify the first and last hit of the track
3. Measure the time difference between these two hits ( $\Delta t$ ).

This method works under the assumptions that the time it takes for a cosmic particle to cross the chamber ( $\sim \text{ns}$ ) is small compared to the charge drift time ( $\sim \text{hundreds of } \mu\text{s}$ ).

We choose cosmic events to allow for a high number of anode to cathode piercing tracks (ACP tracks), rejecting beam events where the particles travel almost perpendicularly to drift direction. We select events with only one reconstructed track to maximize the chance of selecting a single crossing muon (no-michel electron). We utilize ACP tracks because their hits span the full drift length of the TPC, see figure



A.4, allowing us to define where the first and last hit of the tracks are located in space regardless of our assumption of the electric field.

One of the main features of this method is that it doesn't rely on the measurement of the trigger time. Since  $\Delta t$  is the time difference between the first and last hit of a track and we assume the charge started drifting at the same time for both hits, the measurement of the absolute beginning of drift time  $t_0$  is unnecessary. We boost the presence of ACP tracks in the cosmic sample by imposing the following requirements on tracks:

- vertical position (Y) of first and last hits within  $\pm 18$  cm from TPC center (avoid Top-Bottom tracks)
- horizontal position (Z) of first and last hits within 2 and 86 cm from TPC front face (avoid through going tracks)
- track length greater than 48 cm (more likely to be crossing)
- angle from the drift direction (phi in figure A.5) smaller than 50 deg (more reliable tracking)
- angle from the beam direction (theta in figure A.5) greater than 50 deg (more reliable tracking)

Tracks passing all these selection requirements are used for the  $\Delta t$  calculation.

For each track passing our selection, we loop through the associated hits in order to retrieve the timing information. The analysis is performed separately on hits on the collection plane and induction plane, but lead to consistent results. As an example of the time difference, figures A.6 and A.7 represent the difference in time between the last and first hit of the selected tracks for Run-II Positive Polarity sample on the collection and induction plane respectively. We fit with a Gaussian to the peak of the  $\Delta t$  distributions to extract the mean drift time and the uncertainty associated with

it. The long tail at low  $\Delta t$  represent contamination of non-ACP tracks in the track selection. We apply the same procedure to Run-I and Run-II, positive and negative polarity alike.

To convert  $\Delta t$  recorded for the hits on the induction plane to the drift time we utilize the formula

$$t_{drift} = \Delta t - t_{S-I} \quad (\text{A.5})$$

where  $t_{drift}$  is the time the charge takes to drift in the main volume between the cathode and the shield plane and  $t_{S-I}$  is the time it takes for the charge to drift from the shield plane to the induction plane. In Table A.1 we calculated the drift velocity in the S-I region, thus we can calculate  $t_{S-I}$  as

$$t_{S-I} = \frac{l_{S-I}}{v_{S-I}} = \frac{4mm}{1.745mm/\mu s} \quad (\text{A.6})$$

where  $l_{S-I}$  is the distance between the shield and induction plane and  $v_{S-I}$  is the drift velocity in the same region. A completely analogous procedure is followed for the hits on the collection plane, taking into account the time the charge spent in drifting from shield to induction as well as between the induction and collection plane. The value for  $\Delta t_{drift}$ , the calculated drift velocity ( $v_{drift}$ ), and corresponding drift electric field for the various run periods is given in Table A.2 and are consistent with the electric field value calculated with the single line diagram method.

**Delta  $t_{drift}$ , drift  $v$  and E field with ACP tracks**

| Data Period                        | $\Delta t_{Drift} [\mu s]$ | Drift velocity $[mm/\mu s]$ | E field $[V/cm]$ |
|------------------------------------|----------------------------|-----------------------------|------------------|
| RunI Positive Polarity Induction   | $311.1 \pm 2.4$            | $1.51 \pm 0.01$             | $486.6 \pm 21$   |
| RunI Positive Polarity Collection  | $310.9 \pm 2.6$            | $1.51 \pm 0.01$             | $487.2 \pm 21$   |
| RunII Positive Polarity Induction  | $315.7 \pm 2.8$            | $1.49 \pm 0.01$             | $467.9 \pm 21$   |
| RunII Positive Polarity Collection | $315.7 \pm 2.7$            | $1.49 \pm 0.01$             | $467.9 \pm 21$   |
| RunII Negative Polarity Induction  | $315.9 \pm 2.6$            | $1.49 \pm 0.01$             | $467.1 \pm 21$   |
| RunII Negative Polarity Collection | $315.1 \pm 2.8$            | $1.49 \pm 0.01$             | $470.3 \pm 21$   |
| Average Values                     | 314.1                      | $1.50 \pm 0.01$             | $474.3 \pm 21$   |

Table A.2:  $\Delta t$  for the different data samples used for the Anode-Cathode Piercing tracks study.

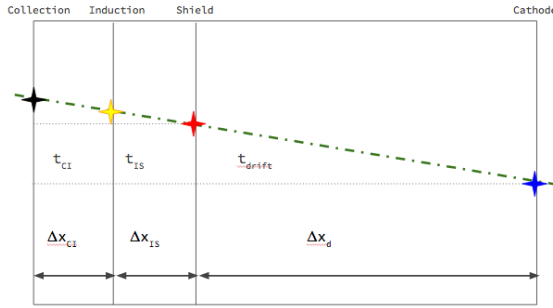


Figure A.4: Pictorial representation of the YX view of the TPC. The distance within the anode planes and between the shield plane and the cathode is purposely out of proportion to illustrate the time difference between hits on collection and induction. A ACP track is shown as an example.

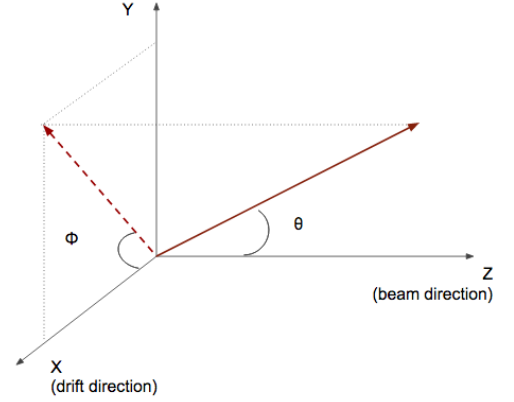


Figure A.5: Angle definition in the context of LArIAT coordinates system.

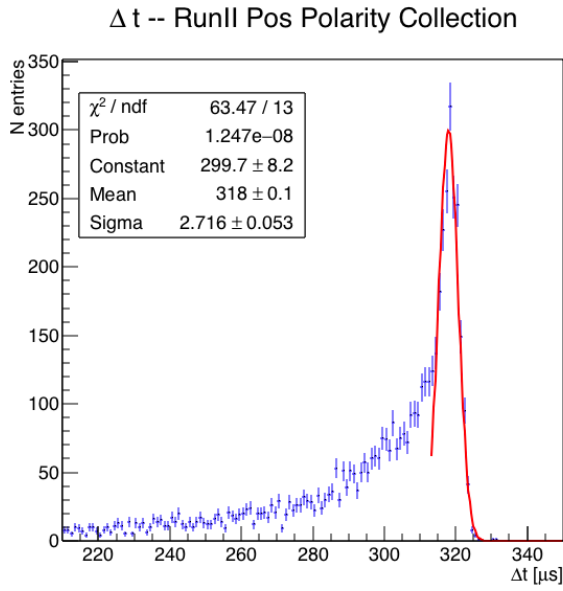


Figure A.6: Collection plane  $\Delta t$  fit for Run II positive polarity ACP data selected tracks.

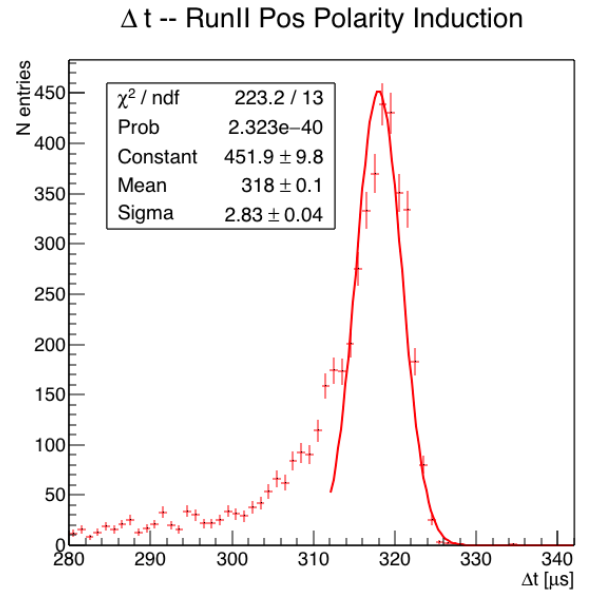


Figure A.7: Induction plane  $\Delta t$  fit for Run II positive polarity ACP data selected tracks.

## Appendix B

### Construction of A Cosmic Ray

### Tagger for MicroBooNE

# Appendix C

## Pion Analysis

### C.0.1 Data Sample

We decided to use only the data from the -60 A, -100 A RunII configurations, because the beam composition for these 2 beamline configurations is available in G4Beamline. Run II data is better than Run I in terms of calorimetry and understanding of the detector.

The used SamWeb definition is PionAna.RunII\_60A\_100A\_lovely1\_e1enag\_00 =

Defined as “defname: Lovely1 and data.tier digits and lariat\_mid\_f.mc7anb ; 0 and create\_date ; '2017-06-02' and run\_number != 9276 and run\_number != 9277 and run\_number != 8836 and run\_number != 9083 and run\_number != 9122 and run\_number != 8977 and run\_number != 8981 and run\_number != 8982 and run\_number != 8983 and run\_number != 8984 and run\_number != 8985 and run\_number != 8991 and run\_number != 8994 and run\_number != 8996 and run\_number <= 8767 and run\_number >= 9635”

### C.0.2 Capture and Decay

Our goal is to measure the total hadronic cross section for negative pions in argon. Since pion capture can be classified as an electromagnetic process and pion decay is

Table C.1: My caption

| Stage                         | -100A +64 GeV | -60A +64 GeV | Number of Evt |
|-------------------------------|---------------|--------------|---------------|
| SamWebDefinition              | 32.7%         | 67.3%        | 3569206       |
| WCQuality                     | 37.8%         | 63.2%        | 553486        |
| $P_{WC4} > 420 \text{ MeV/c}$ | 50.8%         | 49.2%        | 423294        |
| TOF Cut                       | 32.7%         | 67.3%        |               |
|                               |               |              |               |

a week process, capture and decay represent unwanted interactions in our sample. We present here a study of capture and decay in Monte Carlo and the solution we adopted to mitigate their present in our sample.

For this MC study, we use a sample of 359000 MC pions generated according to the beam profile with the DDMC described in 6.1.2. Unlike decay – which may occur both in flight and at rest – capture occurs predominantly at rest. Thus, we can highly mitigate capture and decay at rest by removing pions whose energy is low enough to stop in the TPC. This translates into a momentum selection, where we keep only events whose WC momentum is above a certain threshold. Figure C.1 shows the true momentum distribution for the primary<sup>1</sup> pions that arrive to the TPC (pink), that capture (green) or decay (blue) inside the TPC, on a linear and log scale vertical axis.

In order to choose the selection value for the wire chamber momentum, it is beneficial to estimate the ratio of events which capture or decay that survive the selection in MC as a function of the momentum threshold, and compare it with the survival ratio for all events. This is done in figure C.2. We define the survival ratio simply as the number of events surviving the true momentum cut divided by the number of events of that given category. The survival ratio calculated separately for the three event categories explained above: total (pink), capture (green) and decay (blue). Selecting pions with momentum greater than 420 MeV/c reduces the capture

---

1. We use here the Geant4 denomination "primary" to indicate that the pion considered does not undergo interactions modifying its energy before getting to the TPC. In fact, not every pion shot from wire chamber four will arrive to the TPC as primary, some will decay or interact before the TPC, as explained in [reference to WC 2 TPC chapter](#)

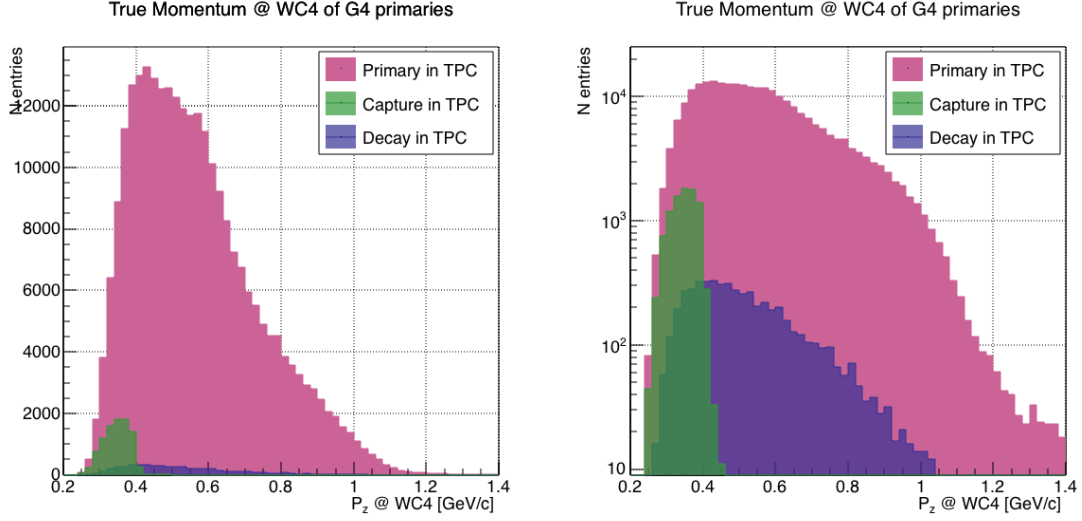


Figure C.1: True momentum distribution at wire chamber 4 for every simulated pion arriving in the TPC (pink), ending its life in capture (green) or in decay (blue) in the TPC, linear vertical axis on the left, logarithmic on the right.

events by 99% while maintaining about 80% of the total data sample. Figure C.3 shows the ratio of events which end their life in capture (green) or decay (blue) over the total number of events as a function of the true momentum at wire chamber four. This ratio is slightly dependent on the inelastic cross section implemented in Geant4, as we are able to register a pion capture (or decay) only if it doesn't interact inelastically in the TPC. For momenta greater than 420 MeV/c, the percentage of capture events drops below 1% and the percentage of decays is never above 2%.



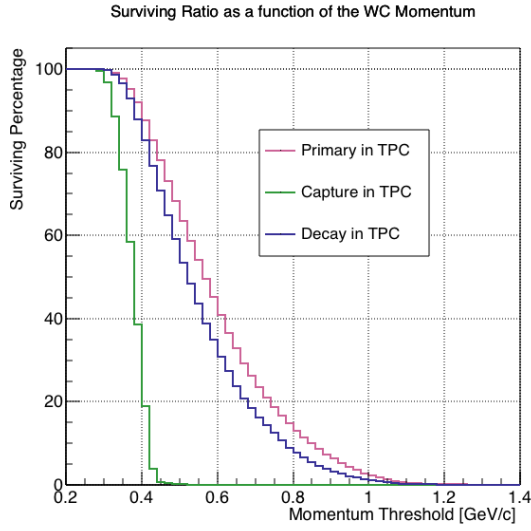


Figure C.2: Survival ratio as a function of selection threshold on true momentum at wire chamber four for every simulated pion arriving in the TPC (pink), capture (green) or in decay (blue).

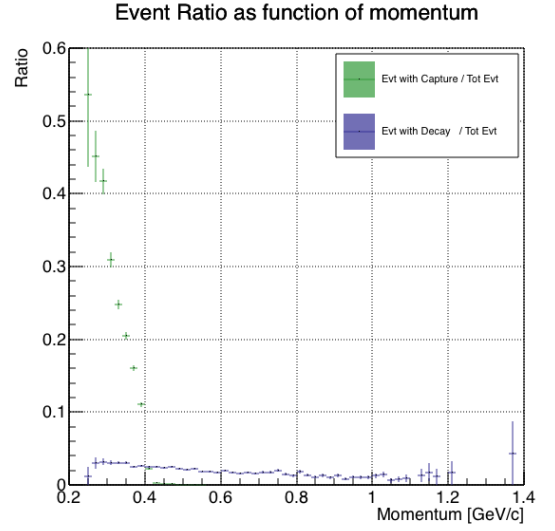


Figure C.3: Ratio between the capture (green) and decay (blue) events over the total number of events as a function of the true momentum at wire chamber four.

# Bibliography

- [1] Peter W. Higgs. Broken symmetries and the masses of gauge bosons. *Physical Review Letters*, 13(16):508–509, oct 1964.
- [2] P.W. Higgs. Broken symmetries, massless particles and gauge fields. *Physics Letters*, 12(2):132–133, sep 1964.
- [3] Steve Ritz et al. Building for Discovery: Strategic Plan for U.S. Particle Physics in the Global Context. 2014.